International Journal of Solids and Structures 51 (2014) 1494–1506

Contents lists available at ScienceDirect

International Journal of Solids and Structures

journal homepage: www.elsevier.com/locate/ijsolstr

Void nucleation and growth in mineral-filled PVC – An experimental and numerical study

Anne Serine Ognedal [a,b,*], Arild H. Clausen [a,b], Torodd Berstad [a,b], Thomas Seelig [c], Odd Sture Hopperstad [a,b]

[a] Structural Impact Laboratory (SIMLab), Norwegian University of Science and Technology (NTNU), Rich. Birkelandsvei 1A, NO-7491 Trondheim, Norway
[b] Department of Structural Engineering, Norwegian University of Science and Technology (NTNU), Rich. Birkelandsvei 1A, NO-7491 Trondheim, Norway
[c] Institute of Mechanics, KIT, Otto-Amman-Platz 9, D-76131 Karlsruhe, Germany

ARTICLE INFO

Article history:
Received 3 September 2013
Received in revised form 2 December 2013
Available online 13 January 2014

Keywords:
Composite materials
Debonding
Plastics
Polymers
Tensile
Tension
Voids
Finite element
Damage
Void nucleation
Void growth
Unit cell simulation
Scanning electron microscopy
SEM
Ductile fracture

ABSTRACT

The nucleation and growth of voids in mineral-filled PVC have been investigated through experimental and numerical studies. Uniaxial tensile specimens were deformed in tension to different elongation levels and then unloaded. The macroscopic strain fields were recorded by use of digital image correlation. After the test, the microstructure of the deformed specimens was investigated in a scanning electron microscope. It was found that the observed volume strain on the macroscale is related to void growth on the microscale. In addition, finite element simulations were performed on unit cell models representing the microstructure of the material in a simplified manner. The numerical simulations demonstrate macroscopic dilation as a result of void growth. Moreover, the numerical simulations indicate that the experimentally observed stress-softening response of the PVC composite material may result from matrix-particle debonding.

1. Introduction

Plastic dilation in polymers can in some cases be related to growth of voids. The presence of voids may give the material a white appearance, which often is referred to as stress whitening. The voids can grow from local irregularities of the molecular packing (Galeski, 2003), from cavitation or debonding of rubber particles (Delhaye et al., 2011) or other particles that are added to the material (Delhaye et al., 2010; Katz and Milewski, 1987). Addition of cheap mineral particles may decrease the cost of the polymer at the same time as it may improve the initial stiffness and the toughness. Particles with proper adhesion to the matrix stay bonded to the polymer matrix at low deformation levels. The particles then act as reinforcement, and the bulk material behaves like a composite material with an increased Young's modulus (Addiego et al., 2011; Kemal et al., 2009; Mishra et al., 1997). However, this depends on how well the particles are bonded to the matrix material (Mishra et al., 1997). Chen et al. (2007) relate the critical stress for particle debonding to the particle size. They show that a higher critical stress is required for smaller particles to debond. However, when the polymer-particle composite material reaches a certain deformation level, also initially well bonded particles debond from the matrix. Debonding of particles gives rise to void growth in the polymer matrix (Delhaye et al., 2010). Thus the load bearing cross section of the material is reduced, resulting in a softening effect on the macroscopic stress–strain curve (Mohanraj et al., 2006). At the same time, the debonding process reduces the plastic resistance of the material (Bartczak et al., 1999; Kemal et al., 2009). In this way brittle behaviour may be avoided, and thus a tougher response can be obtained (Argon and Cohen, 2003).

Finite element analyses of simplified micromechanical models have been used by many researchers to achieve a better understanding of how the presence of particles affects the macromechanical response of polymer materials (Delhaye, 2010; Hempel et al., 2010; Kemal et al., 2009; Pijnenburg and van der Giessen,

* Corresponding author at: Structural Impact Laboratory (SIMLab), Norwegian University of Science and Technology (NTNU), Rich. Birkelandsvei 1A, NO-7491 Trondheim, Norway. Tel.: +47 73594628; fax: +47 73594701.
E-mail address: anne.ognedal@ntnu.no (A.S. Ognedal).

0020-7683/$ - see front matter © 2014 Elsevier Ltd. All rights reserved.
http://dx.doi.org/10.1016/j.ijsolstr.2013.12.042

2001; Seelig and van der Giessen, 2002; Socrate and Boyce, 2000; Steenbrink and van der Giessen, 1999; Steenbrink et al., 1997). It is challenging to reconstruct the complex microstructure of a polymer-particle composite in a finite element mesh. Also, to run simulations on a geometrically realistic model comprising many particles would be computationally rather expensive. It is therefore attractive to represent the real microstructure by simpler geometries in terms of unit cell models. However, since real particles typically have irregular shapes and arrangements, simplifications may affect the results (Williams et al., 2012). The arrangement of the particles may introduce local stress triaxialities and thereby influence the flow behaviour of the matrix material. Moreover, even the molecular structure of the polymer matrix may be affected in case of very small particles (van Dommelen et al., 2003). Another feature is that the stress field around a particle may overlap the stress fields of its neighbours. Socrate and Boyce (2000) report that such interactions between particles become important if the interparticle distance approaches the average particle diameter. In that case, a more advanced micromechanical model such as a 'representative volume element' (RVE) can be used where particles can be organized in a more irregular pattern with a larger variety of particle sizes.

Many of the micromechanical unit cell models found in the literature concern cavitation of soft rubber particles and subsequent void growth. These phenomena are often modelled simply by a matrix material containing initial voids without particles (Pijnenburg and van der Giessen, 2001; Socrate and Boyce, 2000; Steenbrink et al., 1997). Seelig and van der Giessen (2002) modelled a PC with ABS particles, where the rubber phase of the ABS particles was pre-cavitated. In other cases rubber particles are modelled with realistic constitutive models (Delhaye, 2010; Steenbrink and van der Giessen, 1999). Some studies are also performed on polymers containing rigid particles (Delhaye, 2010; Hempel et al., 2010; Kemal et al., 2009; van Dommelen et al., 2003).

Kemal et al. (2009) have studied the toughening of PVC through the addition of nano-particles made of calcium carbonate ($CaCO_3$). They created a unit cell model where they assumed very weak bonding between the particle and the matrix, implying that the particles could be assumed to behave like voids. Another two-dimensional unit cell model representing polypropylene (PP) containing stiff mineral particles in a periodic stacked array and plane strain condition was developed by Delhaye (2010). In this model, the matrix-particle interface was modelled without any bonding.

In polymers, less attention has so far been paid to the debonding process itself. Van Dommelen et al. (2003) used a contact algorithm to describe the interface between rigid particles and a semicrystalline polymer. They presented a study of a two dimensional (plane strain) as well as an axisymmetric RVE representing a semicrystalline polymer containing both soft and stiff particles with different matrix interface strengths. Hempel et al. (2010) studied the effect of different matrix-particle interface strengths in a three dimensional unit cell model representing a PP matrix containing platelet-like talc particles. The matrix-particle interaction was described by a contact algorithm. Cohesive elements allowing for decohesion by normal and tangential separation was also used to describe the void nucleation from debonding of particles. Considering material data for steel, Needleman (1987) used such a cohesive zone model to describe the decohesion of inclusions. Lay et al. (1998) simulated the behaviour of a metal-matrix composite employing a unit cell model with a cohesive zone between the particles and the matrix material. More recent studies are performed, e.g., by Williams et al. (2012).

The macroscopic behaviour of the mineral-filled PVC addressed in this paper has been reported earlier (Moura et al., 2010; Ognedal et al., 2012). The tensile stress–strain curve shows a behaviour that is initially linear elastic before reaching a peak stress, which may be interpreted as a macroscopic yield stress. The peak stress is followed by stress-softening and subsequent re-hardening. Stress whitening and overall volume increase have been observed during plastic deformation. These findings raise two questions to be investigated in the present study:

- Is debonding of particles and subsequent void growth the source of the plastic dilation?
- Is debonding and void growth the cause of the macroscopic stress softening?

In the experimental part of this investigation, test specimens of the mineral-filled PVC have been deformed in tension to different elongations and then unloaded. The in-plane strain fields from the tests were obtained by using digital image correlation (DIC). After testing, the specimens were split in two and investigated in a scanning electron microscope (SEM). The void growth as found from the micrographs was then compared with the dilation of the material on the macroscale. This paper also presents a numerical study of the matrix-particle interaction in a composite material subjected to uniaxial tension. A unit cell model representing a soft polymer matrix containing stiff particles with idealized arrangements and geometries was employed.

2. Mechanical tests

2.1. Material

The test specimens were machined from 10 mm thick plates of extruded PVC. The plates were bought as off-the-shelf products from the producer SIMONA (Product Information PVC-TF). No information about filler content is given in the technical data sheets for the materials. However, thermogravimetric analysis reveals that the material contains 45 wt% solid filler (Ognedal, 2012). Energy dispersive spectroscopy (EDS), which is a built-in tool of the SEM, suggests that most of the observed particles are made of calcium carbonate $CaCO_3$.

2.2. Procedure of tension tests

Ten tensile test specimens with geometry according to Fig. 1 were machined from the extrusion direction of the plates. The thickness was reduced to 4 mm by removing 3 mm material from each side of the plates. The dimensions of the cross sections were measured with a digital sliding calliper before each test.

The loading of the specimens was displacement controlled with a deformation rate of 0.033 mm/s, giving an initial nominal strain rate of $\dot{\varepsilon}_{nom} = 10^{-3}\,s^{-1}$. Each sample was loaded until a certain deformation was achieved. The specimens were then unloaded to zero force at a load rate corresponding to the deformation rate of 0.033 mm/s. Load control was chosen for the unloading to avoid that any compression occurred in the samples. The specimens were left in the testing machine for 10 min after unloading in order to capture possible creep deformations. Two of the ten tests were

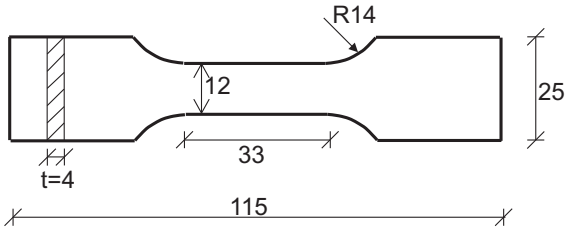

Fig. 1. The geometry of the tensile test specimens. Measures are given in mm.

unsuccessful in the sense that they fractured before unloading. The eight remaining samples were consecutively numbered Test 1 to Test 8 according to their deformation at unloading.

The tests were instrumented with a CCD camera acquiring digital pictures at a frequency of 0.5 Hz. An image was also taken of each specimen before releasing it from the test machine after the creep recovery time of 10 min. This last image was added to the set of images from the test. The strain history from the start of the test until the end of the 10 min creep period could then be found by using DIC. The width and the thickness of the specimens were again measured by a sliding calliper about a week after testing. No further shrinkage was then found.

The longitudinal and transverse strains, here denoted ε and ε_t, respectively, were extracted from the DIC software for the most deformed cross section, i.e., the section experiencing some amount of strain localization and slight necking at the onset of yielding. All strains reported in this article are given as logarithmic strains. Fig. 2 displays a picture of Test 6, Test 7 and Test 8 at the onset of unloading. It is seen that a neck has evolved in these specimens, although it is rather diffuse for Test 6. This introduces a small change in stress triaxiality. However, the stress state is treated as uniaxial throughout the article. By assuming isotropic transverse deformations, the Cauchy stress σ was found as

$$\sigma = \frac{F}{A} = \frac{F}{A_0 \cdot \exp(2\varepsilon_t)} \tag{1}$$

where F is the force as recorded by the test machine, and A and A_0 are the current and the initial cross section area of the specimen. Henceforth σ as defined by Eq. (1) will be called the stress instead of the Cauchy stress.

2.3. Tension test results

The stress–strain curves for the eight successful tests are shown in Fig. 3. The results are in accordance with earlier observations (Moura et al., 2010; Ognedal, 2012). All stress–strain curves show a linear elastic response up to a local stress maximum. The peak stress is followed by softening and subsequent strain re-hardening. Defining the local stress maximum as the yield stress, plasticity sets in at 48–50 MPa, with a minor variation between the tests. The corresponding longitudinal strain is around 0.035. A gradual increase of stress whitening was visually observed around onset of yielding.

The volume strain is calculated as $\varepsilon_v = \varepsilon + 2\varepsilon_t$, assuming that the transverse strains in the width and thickness directions are the same (Moura et al., 2010). Fig. 4(a) shows the volume strain plotted against longitudinal strain. There is some variation between the curves in the figure. However, plastic dilation is clearly present in the tests. From the figure it can be seen that the volume strain does not increase linearly with the longitudinal strain. The curves have a slightly convex shape.

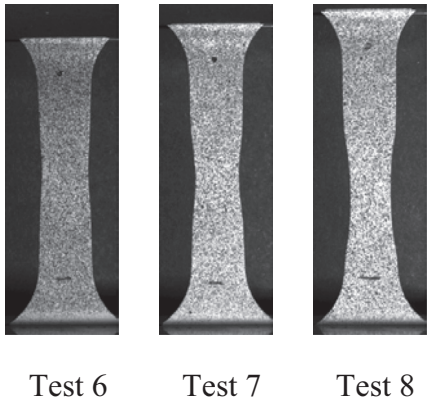

Fig. 2. Three test specimens immediately before unloading.

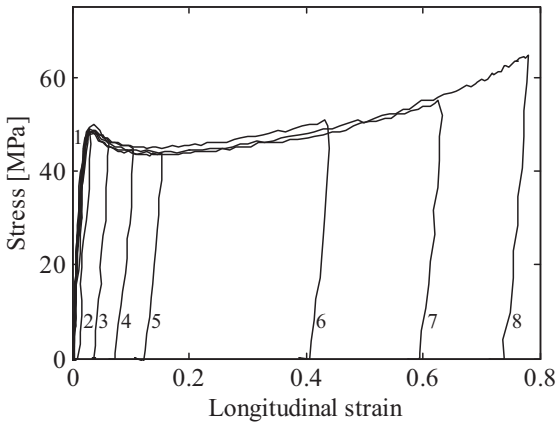

Fig. 3. Cauchy stress vs. longitudinal strain curves for Test 1 to Test 8. The plot includes the loading and unloading stages as well as creep recovery after the test.

The nonlinear evolution of the dilation becomes clearer when looking at Fig. 4(b), representing the retraction ratio, defined as $\rho = -\varepsilon_t/\varepsilon$, plotted against the plastic longitudinal strain, $\varepsilon^p = \varepsilon - \sigma/E$, where E is Young's modulus. Since noise in the strain measurements causes fluctuations in the retraction ratio, the curves have been smoothed to improve the representation. It is seen that the retraction ratio has a minimum at a plastic longitudinal strain of 0.04–0.06, corresponding to a total longitudinal strain of 0.07–0.10. This is where the increase of dilation is largest, see Fig. 4(a). The retraction ratio increases, i.e., the increase in dilation decays, when the plastic longitudinal strain exceeds about 0.1. At unloading, there is a difference in the evolution of the retraction ratio between the tests. The retraction ratio remains almost constant, or exhibits a slight increase, during unloading of the highly stretched specimens, i.e., Test 6 to Test 8, while it has a significant decrease during unloading of the other specimens.

3. SEM investigation

3.1. Specimen preparation for SEM

The stress–strain curves in Fig. 3 were determined from the DIC measurements of the most deformed cross section. Small pieces containing this part of the samples were cut out for the post-test SEM investigation. These pieces were stored in liquid nitrogen at −196 °C for 30 min to facilitate brittle fracture and avoid undesired deformations during the fracture process. Thereafter they were split in two in the longitudinal direction. This process ensured brittle fracture with two longitudinal fracture surfaces as a result. One such fracture surface from each test specimen was chosen for microscopic examination.

Prior to the SEM investigation, the surface of the specimen was coated with carbon dust by an Agar Turbo Carbon Coater. The location for highest straining was thereafter investigated in a SEM of type Zeiss Supra 55VP.

3.2. Results from SEM investigation

Two micrographs from each test specimen were investigated, each covering an area of 38.6 μm × 26.0 μm. A section from a scanning electron micrograph of undeformed PVC is displayed in Fig. 5. As for the deformed samples, it was cooled in liquid nitrogen

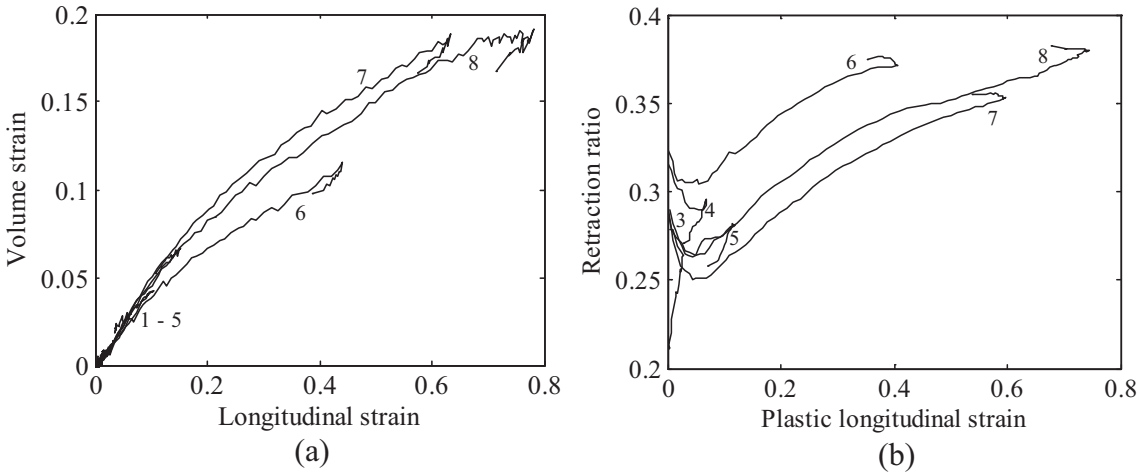

Fig. 4. (a) Volume strain plotted against longitudinal strain for Test 1 to Test 8. (b) Retraction ratio plotted against plastic longitudinal strain for Test 3 to Test 8. Both plots include the loading and unloading stages as well as creep recovery after the test.

before it was split in two. Image analysis suggests that the material contains a volume fraction ω_0 of particles around 0.24. The exact mass density of the constituents of the filled PVC is not known. Still, this value seems to be in reasonable correspondence to the weight fraction of 0.45 found by the thermogravimetric analysis mentioned before. Judged from their visual appearance, two kinds of particles might be present. There are some rather spherical particles that are comparatively small, having diameter around 0.2–0.4 μm, and some larger particles having a more irregular shape. Both kinds of particles exhibit a distribution of size. The dispersion of particles in the matrix material appears to be good. Some empty holes can be seen in the micrograph displayed in Fig. 5. It is assumed that these were occupied by particles before the specimen was split in two.

Energy dispersive spectroscopy (EDS) on the larger irregular particles suggests that the filler is made of $CaCO_3$. We can therefore expect that the particles are relatively stiff compared to the PVC matrix. The spherical particle type was too small for EDS analysis.

Representative micrographs for the specimens of Test 1 to Test 8 are presented in Fig. 6. In all cases, the vertical direction of the micrographs represents the tensile direction. The sample from Test 1 was only deformed elastically. Test 2 was unloaded at peak stress, see Fig. 3, in other words at onset of macroscopic yielding. No voids are observed around any of the particles in the samples from Test 1 and Test 2. Nevertheless, the particles might have debonded from the matrix. If debonding takes place before the material yields, the void growth is elastic and the void might enclose the particle during unloading. In the micrograph of Test 3 and Test 4 we can vaguely see the first evidence of matrix–particle separation causing formation of voids around some particles. The debonding seems to occur around the large particles first. However, the voids are not very clear at this stage. Between Test 4 and Test 5 there is a marked difference in the appearance of the voids, even though the difference in strain level, see Fig. 3, between these two tests is moderate. In the micrographs from Test 5 many of the particles have clearly debonded from the matrix, and it is apparent that the void size has increased around the particles. Also in the micrograph of the specimen from Test 6 we can clearly see how voids have grown around the particles. In the two most deformed specimens, Test 7 and Test 8, a larger amount of the particles have debonded from the matrix and the voids are considerably larger than in the other micrographs.

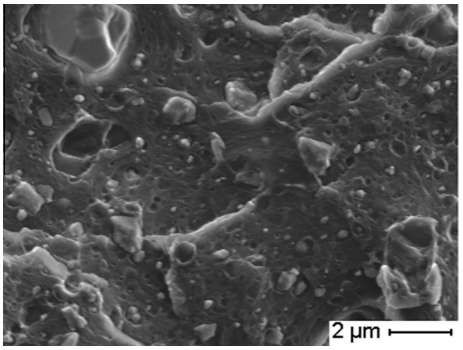

Fig. 5. Microstructure of undeformed mineral-filled PVC.

3.3. Estimation of void volume fractions

The contours of the areas containing particles and voids in the SEM micrographs were traced manually. It was in many cases hard to distinguish particles from voids. Moreover, it was impossible to determine whether a void used to contain a particle before the specimen was split in two. Therefore, particles and voids were together identified as one object type. The area fraction of particles and voids ω_A was determined from the manually traced boundaries by using the open-source image processing and analysing program ImageJ (Schneider et al., 2012). The principle of Delesse (Addiego et al., 2011; Weibel, 1979), stating that the area fraction ω_A of a component in a random cross section is equal to the volume fraction ω of the component in the entire material, was then employed. This principle also holds for anisotropic objects. The only requirements are that the cross section has to be typical and selected by random.

It was assumed that the undeformed PVC contained no voids, only particles. The fraction of objects observed in a micrograph of the undeformed material, ω_0, was therefore assumed to represent the particle content of the material.

Particle and void volume fractions ω were estimated by exploring two micrographs from each of the eight tests. Fig. 7(a) shows the volume fractions ω plotted against the plastic longitudinal strain at the end of the test, including the 10 min creep recovery time. It is clearly seen that ω increases with the longitudinal plastic strain, indicating void growth.

We assume that particle debonding is the only source of void nucleation. This means that the voids are created only around

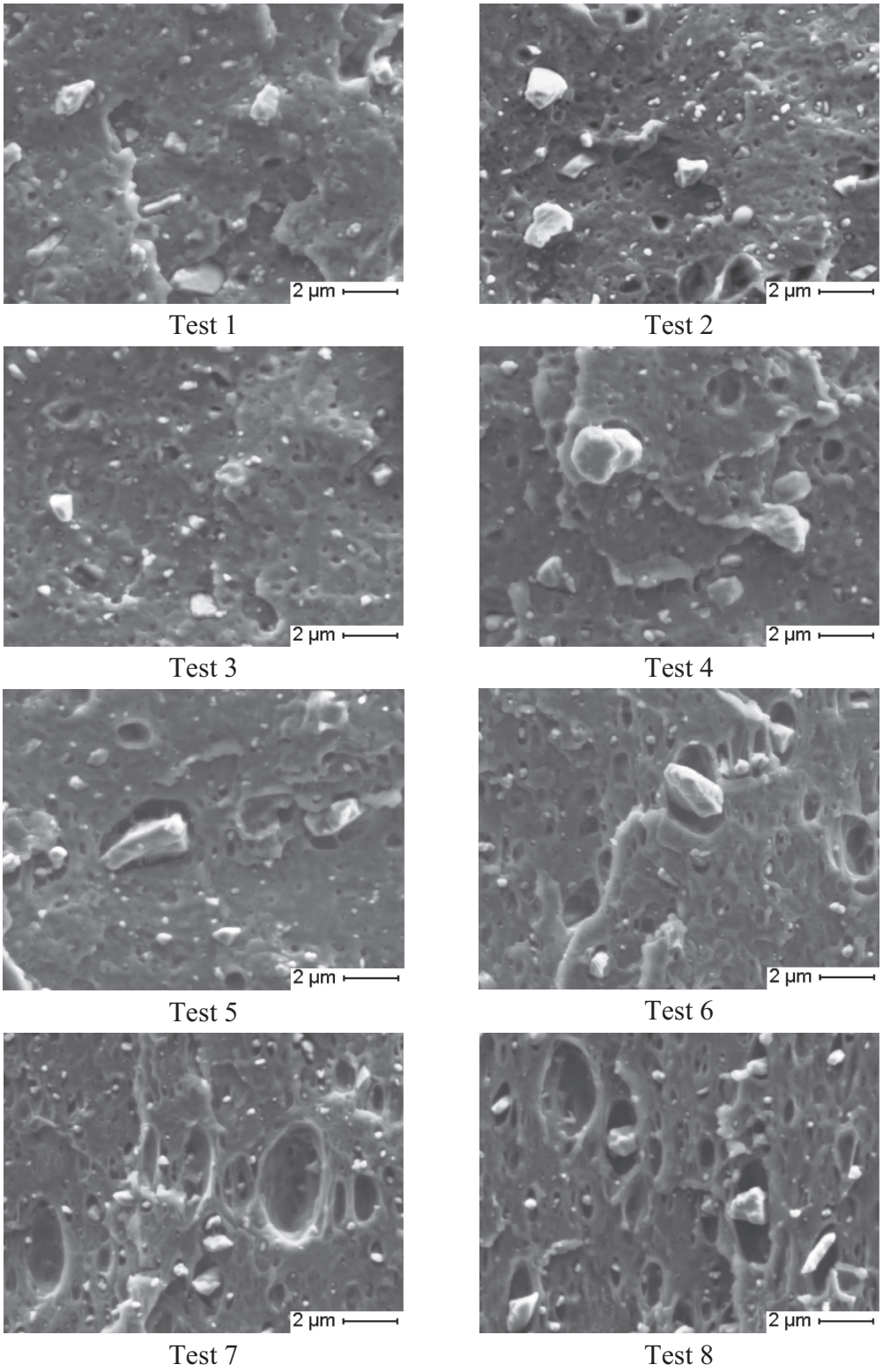

Fig. 6. Microstructure of deformed test specimens of mineral-filled PVC.

the particles. Ignoring other sources of nucleation, the evolution of the particle and void volume fraction $\dot{\omega}$ can be written

$$\dot{\omega} = \dot{\omega}_g \tag{2}$$

where $\dot{\omega}_g$ is the increase of the combined particle and void volume fraction. Further, $\dot{\omega}_g$ can be expressed through the plastic volume strain rate $\dot{\varepsilon}_v^p$ as

$$\dot{\omega}_g = (1-\omega)\dot{\varepsilon}_v^p \tag{3}$$

by assuming an incompressible matrix. By integrating this differential equation we can describe the plastic volume strain in terms of the particle and void volume fraction ω, viz.

$$\varepsilon_v^p = \ln\left(\frac{1-\omega_0}{1-\omega}\right) \tag{4}$$

From the micrograph of the undeformed sample, the initial void and particle fraction ω_0 was found to be 0.24. Eq. (4) was then used to calculate values of ε_v^p from the estimates of ω. The results are plotted with triangles in Fig. 7(b). In the same figure, the volume strains measured by DIC at the end of 10 min of creep after the test are plotted with crosses. It is seen that the volume strains predicted by employing Eq. (4) on the SEM data, i.e., the estimated values of ω, are close to the volume strains measured by DIC. The deviation may be related to some inaccuracies in the SEM data, especially for the undeformed sample. The SEM data at hand suggests that the undeformed sample has a higher value of ω than some of the deformed specimens. As a result, some faulty negative volume strains are predicted. Yet, the gradient of the volume strain with increasing deformation is rather well captured.

3.4. Estimation of effective stress in the matrix ligaments

To investigate the damage effect in terms of loss of strength of the composite material, it is of interest to establish an expression for the volume fraction ω_D, which represents the sum of the volume fractions of debonded particles and the surrounding voids. In other words, the volume occupied by a debonded particle is included in ω_D. The volume occupied by particles that are still attached to the matrix is not included in ω_D since these particles carry load. The particles in our material seem to have a good initial bonding to the PVC matrix, therefore it is likely that the initial volume fraction of damaged material is $\omega_D = 0$. We then assume that the particles act as nucleation sites when a critical stress is reached, and ω_D rapidly starts to increase. The volume fraction of material that is damaged by nucleated voids is denoted $\omega_{D,n}$. If we assume that all particles are debonded after a certain deformation, and that particle debonding is the only nucleation process, we get an upper limit of $\omega_{D,n}$ that is determined by the particle content of the material. In addition, the already nucleated voids grow. This gives rise to another contribution to the damage volume fraction that is denoted $\omega_{D,g}$. The total increase of void volume fraction ω_D is therefore the sum of two contributions

$$\dot{\omega}_D = \dot{\omega}_{D,n} + \dot{\omega}_{D,g} \tag{5}$$

During testing, it was visually observed that stress whitening started around peak stress. This indicates that the particle debonding also is initiated at this stage. We therefore assume that the nucleation of voids starts at onset of plasticity, when $\varepsilon^p = 0$. From Fig. 4(b) it is seen that the increase in dilation decays when the retraction ratio is at a minimum around $\varepsilon^p \approx 0.07$, i.e., at a strain level of $\varepsilon \approx 0.10$. It is assumed that no more voids can nucleate after this strain level. Thus, the following simple model describing volume fraction of nucleated voids is proposed

$$\omega_{D,n} = \omega_0[1 - \exp(-50\varepsilon^p)] \tag{6}$$

The particle volume fraction $\omega_0 = 0.24$ is considered as the upper limit for the void nucleation process. The factor 50 ensures that the nucleation process terminates around $\varepsilon = 0.10$. Differentiation of Eq. (6) gives the following expression for void nucleation on rate form

$$\dot{\omega}_{D,n} = 50\omega_0 \exp(-50\varepsilon^p)\dot{\varepsilon}^p \tag{7}$$

The contribution for void growth is given by Eq. (3) and reads as

$$\dot{\omega}_{D,g} = (1 - \omega_D)\dot{\varepsilon}_v^p \tag{8}$$

By employing Eq. (5) with Eqs. (7) and (8) on data from Test 8, we obtain the evolution of damage ω_D presented in Fig. 8(a). As described when proposing Eq. (6), the nucleation process ceases at a strain around 0.1. The contribution from the void growth term increases continuously during the test.

Debonding and void growth reduce the load carrying cross section of the specimen. An estimate of the effective stress σ_{eff}, regarded as the average stress in the ligaments between the debonded particles and the voids (Kachanov, 1986; Mohanraj et al., 2006), can be expressed as

$$\sigma_{eff} = \frac{\sigma}{1 - \omega_D} \tag{9}$$

The solid line in Fig. 8(b) represents the effective stress of the damaged composite according to Eq. (9). It is seen that there is no drop in the effective stress with straining. The dashed thin line in Fig. 8(b) represents the stress–strain curve from Test 8 without taking damage from debonding and void growth into account.

4. Numerical study

4.1. Finite element discretization

A unit cell model was set up to represent a material with a particle volume fraction of $\omega_p = 0.2$. This figure corresponds to the fraction in the mineral-filled PVC at hand. The particles are modelled as spheres arranged in a staggered array, see Fig. 9(a) which shows an assembly of eight unit cells. Eight-node solid elements

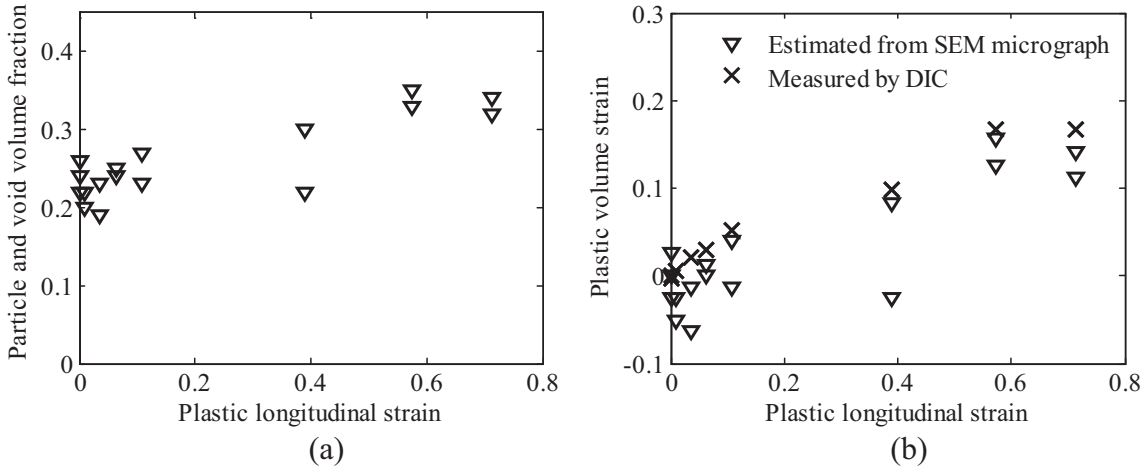

Fig. 7. (a) Particle and void volume fractions, as estimated from scanning electron micrographs, plotted against plastic longitudinal strain. (b) Plastic volume strain plotted against plastic longitudinal strain. The triangles represent plastic volume strain estimated from SEM in conjunction with Eq. (4) and the crosses refer to plastic volume strain measured by DIC at the end of the test.

with reduced integration were used for the mesh depicted in Fig. 9(b). A layer of cohesive elements, described below, was introduced between the particle and the matrix with the aim to represent the matrix-particle interface. Two different meshes consisting of 17,600 and 52,650 elements were considered.

The numerical simulations in the present work were carried out by the explicit solver of the commercial finite element code LS-DYNA (LS-DYNA, 2007). It was checked for all simulations that the kinetic energy was negligible compared to the external work done on the unit cell.

4.2. Material models

A rather simple material model featuring linear elasticity and finite strain J_2 plasticity with isotropic hardening was used to model the matrix material. Hence, strain rate and temperature dependence – though generally important in the deformation behaviour of polymers – are not considered in the present study. The literature reports that a stress-softening behaviour, or intrinsic softening, can be observed in PVC without filler (G'Sell et al., 1992). However, the PVC-matrix in the current study is modelled without intrinsic softening in order to isolate the effects of particle debonding and void growth. The Young's modulus E_m of the matrix material of a composite with rigid spherical particles can be estimated from (Fu et al., 2008)

$$E_m = \frac{E_c}{(1+2.5\omega_p)} \tag{10}$$

where E_c is Young's modulus of the composite material and ω_p is the volume fraction of particles. This estimate is valid only for low particle volume fractions (Fu et al., 2008). However, it is regarded as sufficiently accurate for the present purpose. From the data sheet provided by the supplier it was found that $E_c = 3000$ MPa. With a volume fraction $\omega_p = 0.2$, Young's modulus for the matrix material is obtained as $E_m = 2000$ MPa. The Poisson's ratio for the matrix material was set to $\nu_m = 0.3$. The initial matrix yield stress of $\sigma_T = 60$ MPa and the post-yield hardening behaviour of the matrix material were adapted to match the effective stress data according to Eq. (9) under uniaxial tension. Fig. 8(b) includes the stress–strain curve for the matrix material along with the effective stress computed from Eq. (9) and the composite response from the experimental test denoted Test 8. The $CaCO_3$ particles were modelled as elastic with the properties $E_p = 35{,}000$ MPa and $\nu_p = 0.2$ (Vollenberg and Heikens, 1990).

4.3. Modelling of matrix–particle interface

The interface between the matrix and the particles was modelled with cohesive elements in order to simulate matrix-particle debonding. The response of the cohesive elements is specified by a bi-linear traction-separation law which uses a damage formulation and a mixed-mode delamination criterion (Material type 138 in LS-DYNA). In this study, identical behaviour in the normal and the tangential direction is assumed for simplicity. Let t_I and t_{II} be the tractions and δ_I and δ_{II} the separations in the normal direction (mode I) and the tangential direction (mode II), respectively. The effective traction t and the effective mixed-mode opening displacement δ are then defined as

$$t = \sqrt{\langle t_I \rangle^2 + t_{II}^2}, \quad \delta = \sqrt{\langle \delta_I \rangle^2 + \delta_{II}^2} \tag{11}$$

where $\langle x \rangle = (x + |x|)/2$ denotes the positive part of the argument. The traction-separation law in the space defined by t and δ is specified in terms of the initial stiffness k, the cohesive strength T, and the fracture toughness G_c as illustrated in Fig. 10. The effective mixed-mode opening displacement at damage initiation is defined as

$$\delta_0 = \frac{T}{k} \tag{12}$$

The ultimate mixed-mode opening displacement is given by the Benzeggagh-Kenane law (LS-DYNA, 2007) which reduces to

$$\delta_f = \frac{2G_c}{k\delta_0} \tag{13}$$

due to the identical behaviour in the normal and tangential directions. When the mixed-mode opening displacement δ reaches δ_f, the cohesive element is eroded. Note that the cohesive law also incorporates irreversible partial debonding and intermediate unloading with a reduced (i.e., damaged) secant stiffness as sketched by the dashed line in Fig. 10, see also (LS-DYNA, 2007). The linear initial stiffness k of the cohesive elements is defined in terms of Young's modulus of the matrix material E_m and the cohesive element thickness h_{int} as $k = E_m/h_{\text{int}}$. The thickness h_{int} of the cohesive layer is 1/500 of the initial length of the unit cell. Variations in the matrix-particle interface strength, as considered in the numerical simulations below, are controlled by defining different values of the cohesive strength T and the fracture toughness G_c. Given the cohesive strength T, the fracture toughness G_c is defined so that the ultimate mixed-mode opening displacement δ_f is four

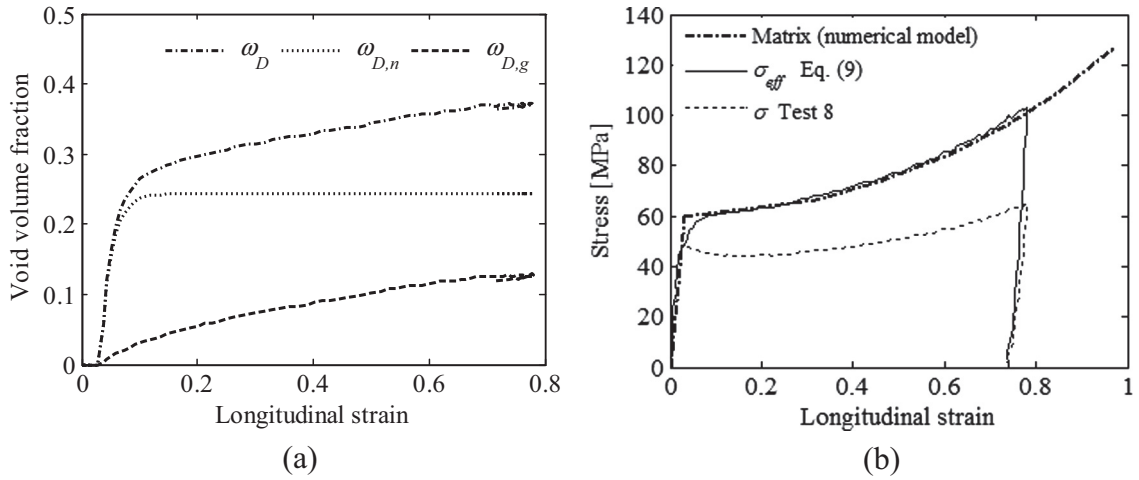

Fig. 8. (a) Estimate of the evolution of void volume fraction of debonded particles and surrounding voids for Test 8. (b) Estimate of effective stress in the matrix ligaments between the voids vs. longitudinal strain. The figure also includes the stress–strain curve under uniaxial tension adopted for the matrix material in the unit cell model.

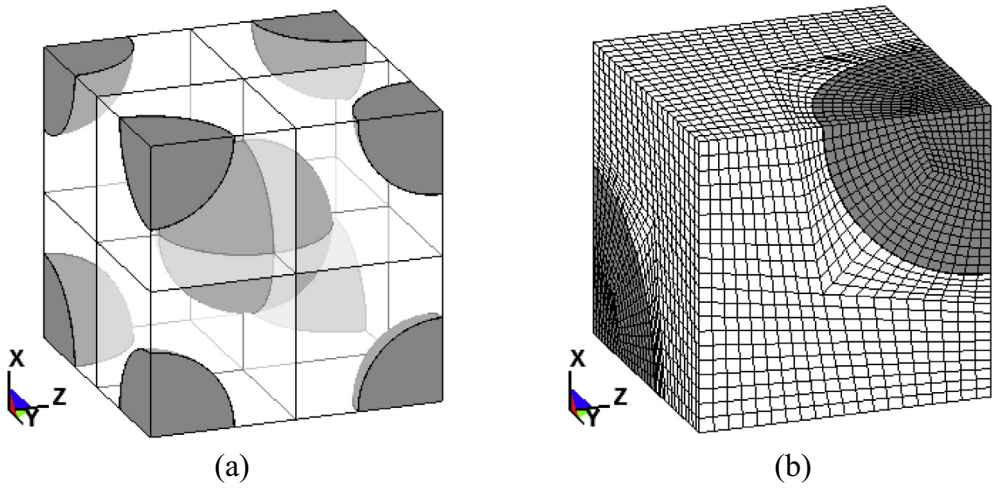

Fig. 9. The unit cell model representing a staggered array of spherical particles with a particle volume fraction of $\omega_p = 0.2$. (a) Assembly of eight unit cell models. (b) Finite element mesh of one unit cell consisting of 17,600 elements.

times the effective mixed-mode opening displacement at damage initiation δ_0 in all simulations. A contact algorithm without friction (LS-DYNA, 2007) is employed for the matrix-particle interaction after erosion of the cohesive elements. For further details on cohesive elements the reader is referred to, e.g., Pinho et al. (2006).

4.4. Results from numerical unit cell study

Macroscopic uniaxial tension of the cubic unit cell was specified by prescribing equal normal displacements to the nodes on the surface facing the positive x-direction, see Fig. 9(b), while the nodes on the lateral surfaces were constrained to planar movement with zero resultant normal forces. Due to symmetry, shear stresses are zero at the unit cell surface. Note, that under this kind of loading and boundary conditions the unit cell model features periodicity.

In order to represent the overall behaviour of the unit cells, the terms macroscopic stress and macroscopic strain are used. The macroscopic stress is a "macroscopic Cauchy stress" calculated by dividing the force acting at the cross section of the unit cell by the current area of the cross section. The macroscopic strains are calculated as the logarithmic strains computed from the lengths of the edges of the unit cell.

Two initial test simulations, one using a mesh with 17,600 elements and one with a finer mesh with 52,650 elements, were carried out in order to analyze the mesh dependence of the results.

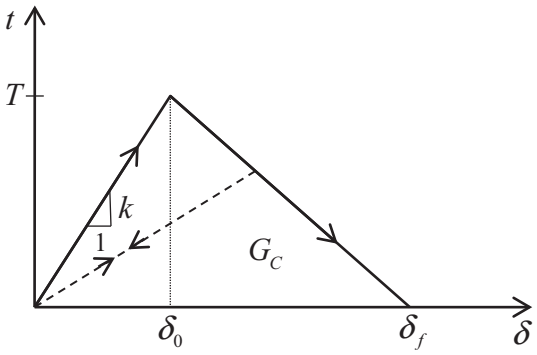

Fig. 10. Illustration of the bi-linear traction-separation law for the cohesive elements.

The cohesive strength was set to $T = 74$ MPa in these simulations. It is seen in Fig. 11 that there is not much difference in the results with the fine and the coarse mesh. The coarse mesh has therefore been used in the following.

Matrix-particle debonding can be observed as a rather sudden drop in the macroscopic stress–strain curves in Fig. 11. Compared with the experimental data from the tests, see Fig. 3, the stress drop predicted by the unit cell model appears too sudden. However, since the matrix-particle interface strength can be related to the size of the particle (Chen et al., 2007), and it appears from the SEM images in Figs. 5 and 6 that particles of different size are present in our material, it is probable that there is some variation in the matrix-particle interface strengths. Let us in the following assume that the real material behaves as a combination of many unit cell models, each with a different cohesive strength T of the particle matrix interface. Lay et al. (1998) used a normal distribution of the cohesive strength in order to model more realistic behaviour of a composite. A normal distribution of the cohesive strength T can be expressed as

$$f(T) = \frac{1}{s_T\sqrt{2\pi}} \exp\left(\frac{-(T - T_{mean})^2}{2s_T^2}\right) \tag{14}$$

where T_{mean} denotes the mean cohesive strength and s_T is the standard deviation. The stress interval between 63 MPa and 87 MPa was divided into twelve classes with a class interval of 2 MPa. Each of the classes was represented by a unit cell simulation with cohesive strengths T of 64 MPa, 66 MPa, ..., 86 MPa. The results from these simulations are shown by the dashed lines in Fig. 12(a).

A normal distribution of cohesive strengths in the range 63 MPa to 87 MPa was created from Eq. (14) with mean cohesive strength set to $T_{mean} = 75$ MPa and the standard deviation to $s_T = 4$ MPa. The normal distribution was used to create a set of twelve weighting factors W_i, where $i = 1, \ldots, 12$ and $\sum_{i=1}^{12} W_i = 1$, for the twelve classes. The weighting factors are presented in Fig. 12(b). With this distribution it is assumed that a small fraction of the real composite behaves like the unit cell models with cohesive strengths of 64 MPa and 86 MPa. On the other hand, a rather larger fraction of the real composite is represented with unit cell models defined by cohesive strengths 74 MPa and 76 MPa, while the remaining eight cohesive strengths have intermediate weighting factors in accordance with Fig 12(b).

All unit cell simulations were deformation controlled. This means that the evolution in macroscopic longitudinal strain is

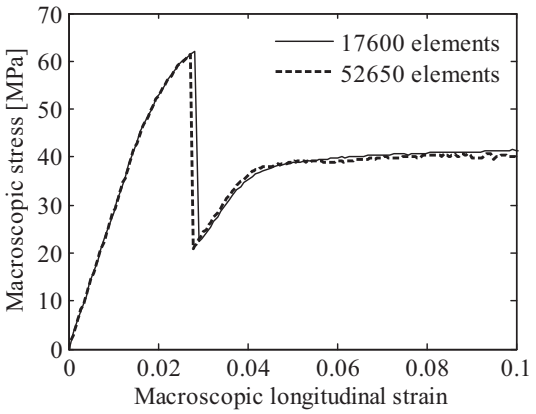

Fig. 11. Results from unit cell model simulations with fine and coarse mesh.

equal for all simulations. However, due to the differences in cohesive strengths, the macroscopic stress level evolves differently. This is clearly seen in Fig. 12(a). By employing the weighting factors in Fig. 12(b), a weighted stress $\hat{\sigma}$ for each strain level ε from the simulations was computed as

$$\hat{\sigma}(\varepsilon) = \sum_{i=1}^{12} W_i \sigma_i(\varepsilon) \tag{15}$$

where $\sigma_i(\varepsilon)$ represents the macroscopic stresses from the twelve individual unit cell simulations at a certain strain level. The weighted macroscopic stress–strain curve calculated with Eq. (15) is represented by the bold solid line in Fig. 12(a). It is seen that behaviour much closer to the experimental data is obtained when we take a variation of cohesive strengths into consideration.

Well dispersed particles of same constitution, shape and size create similar conditions at the matrix-particle interfaces (Chu and Needleman, 1980). It is reasonable to expect a low scatter of matrix-particle interface strengths in such a material. On the other hand, it can be assumed that a material with a great variation in the particle size exhibits a large scatter of critical interface strengths between the matrix and the particles. It is interesting to investigate how different distributions of cohesive strengths affect the shape of weighted stress–strain curve. Six new sets of weighting factors were created employing different values of mean cohesive strength T_{mean} and standard deviation s_T. Additional simulations were also carried out to extend the interval of cohesive strengths to the range from 58 MPa to 92 MPa. In a similar manner as described with Eq. (15), weighted stress–strain curves were created from different cohesive strength distributions defined by Eq. (14). The results are shown in Fig. 13. Fig. 13(a) demonstrates that an increase in the mean cohesive strength T_{mean} leads to a higher value of maximum stress for the weighted stress–strain curve. Here, the standard deviation s_T is kept constant. In Fig. 13(b), where T_{mean} is kept constant and s_T is varied, it is seen that a narrower distribution represented by the dashed line leads to an increase in the peak stress and a more pronounced stress softening. Similar results are found by Lay et al. (1998).

Fig. 14 shows the void growth around a particle in the unit cell model with cohesive strength of 74 MPa. The deformation occurred in this manner also for the unit cell models with other cohesive strengths. After the particle has debonded from the matrix, void growth leads to increase of volume strain on the macroscale. The macroscopic volume strains from the 12 unit cell simulations in the stress interval between 63 MPa and 87 MPa are plotted by dashed lines in Fig. 15. Similar as for the stress, a weighted volume strain $\hat{\varepsilon}_v$ was computed as

$$\hat{\varepsilon}_v(\varepsilon) = \sum_{i=1}^{12} W_i \varepsilon_{v,i}(\varepsilon) \tag{16}$$

Here, $\varepsilon_{v,i}(\varepsilon)$ is the volume strain in each of the twelve unit cell simulations at strain level ε, and the weighting factors W_i are given in Fig. 12(b). The bold line in Fig. 15 represents the weighted volume strain, again adopting a mean cohesive strength of 75 MPa and a standard deviation of 4 MPa. Comparing the numerical results with the thin continuous line, representing the volume strain measured in the experiment, it is seen that all unit cell simulations underestimate the volume strain.

In addition to the simulations for different matrix-particle interface strengths, two further simulations were carried out, one for a unit cell representing mineral-filled PVC with zero interface strength and one for a unit cell without particle, i.e., containing just a void. The purpose was to study how the mere presence of particles and voids affects the deformation. The results from these simulations are shown in Fig. 16 in comparison with the result from the unit cell model with cohesive strength of 74 MPa. The macroscopic stress–strain curves in Fig. 16(a) show that there is not

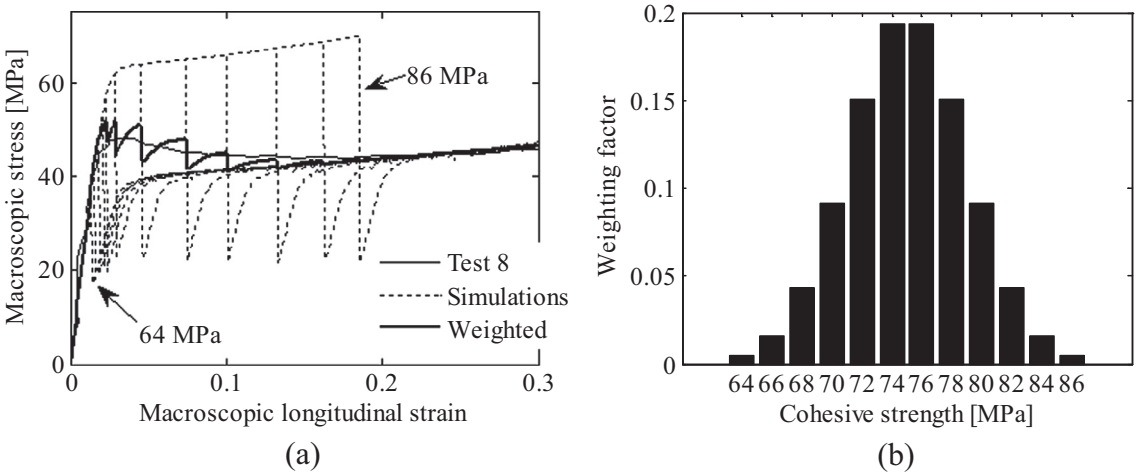

Fig. 12. (a) Macroscopic stress–strain curves from numerical simulations on unit cell models with cohesive strengths 64 MPa, 66 MPa,..., 86 MPa and a weighted stress–strain curve where the data from the different numerical simulations have been multiplied with normal distributed weighting factors. Also shown is the experimental stress–strain curve from Test 8. (b) Weighting factors for the 12 different cohesive strengths used in the numerical unit cell simulations. Mean cohesive strength is T_{mean} = 75 MPa and standard deviation is s_T = 4 MPa.

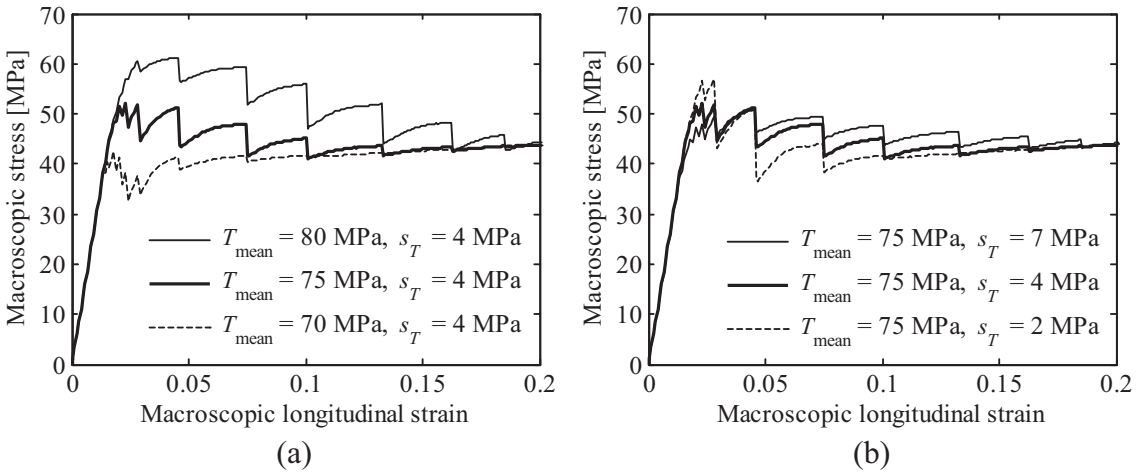

Fig. 13. Weighted macroscopic stress–strain curves showing the effect of different (a) mean cohesive strengths and (b) standard deviations.

much difference between the model with zero matrix-particle interface strength and the model without particles. In both cases, the initial response is softer than for the unit cell model with an initially well bonded particle. Whether the material contains unbonded particles or voids does not seem to affect the stress–strain curve in uniaxial tension. However, from the evolution of volume strain in Fig. 16(b) it is seen that the presence of particles has an effect. Significantly larger volume strain can be expected in a material that contains stiff particles compared to a voided material since the particles prevent the lateral contraction of voids.

5. Discussion

5.1. Experimental study

Specimens of PVC filled with $CaCO_3$-particles were loaded in uniaxial tension up to different elongations and thereafter unloaded. The most deformed zones of the specimens were investigated in SEM after testing in order to study how the morphology of the composite changes with the deformation. Initially the $CaCO_3$ particles appear to be well bonded to the PVC matrix. However, it is

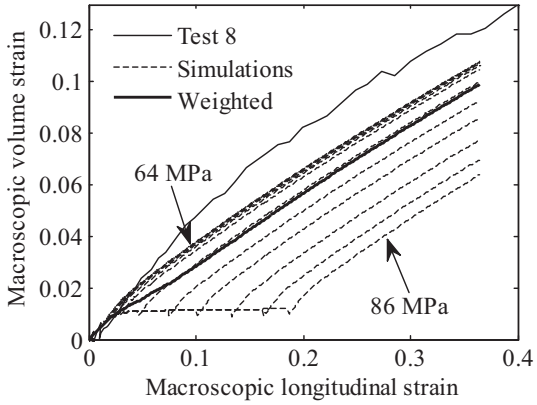

Fig. 15. Macroscopic volume strain curves from numerical simulations on unit cell models with cohesive strengths 64 MPa, 66 MPa, . . ., 86 MPa and weighted volume strain curve where the data from different simulations have been multiplied with the normal distributed weighting factors in Fig. 12(b), with mean cohesive strength of 75 MPa and standard deviation of 4 MPa. Also shown is the volume strain from experimental Test 8.

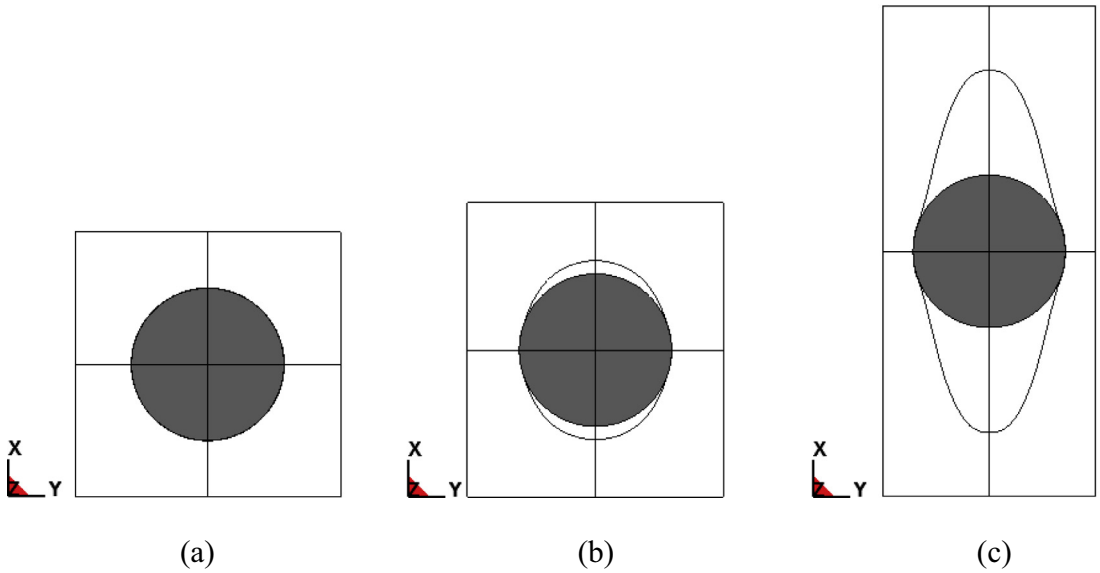

Fig. 14. Section view of unit cell model displaying void growth around a particle at macroscopic longitudinal strains of (a) 0, (b) 0.1 and (c) 0.6.

clearly seen from Fig. 6 that the particles debond from the matrix at larger deformations. The particles act as nucleation sites for voids that continuously grow as the material deforms, causing an overall volume increase.

Volume fractions of particles and voids found from analyzing two micrographs from each test specimen were employed to estimate the plastic volume strain. The result from these microscopic measurements is, according to Fig. 7(b), in good agreement with the volume increase at the macroscopic scale as measured by DIC. It is therefore reasonable to conclude that the main reason for the macroscopic dilation is void growth on the microscopic scale. Volume increase in polymers due to void growth is commonly reported in the literature. Some examples from recent studies are Laiarinandrasana et al. (2012) and Cayzac et al. (2013). Additional aspects, such as molecular packing caused by orientation of amorphous chain segments (Cangemi et al., 2004) or nucleation of voids in lesser dense packed areas (Galeski, 2003), might also affect the volume change. Indeed, Guo et al. (2008) separate between intrinsic dilation, e.g., from change of the free volume of the polymer, and extrinsic dilation related to void growth. However, the intrinsic dilation is assumed to be of minor importance in the mineral-filled PVC considered in the current study and will not be further discussed here.

There are several possible sources of error in the particle and void identification process. The splitting of the specimens for SEM inspection does not create an entirely planar surface since the fracture imposed during splitting follows the "easiest way" through the specimen. The surface investigated in the SEM may therefore have contained a higher density of voids than what is representative for the whole specimen. On the other hand, this may be assumed to be the case of all samples. If so, the evolution of volume strain should be rather unaffected. Moreover, splitting of the specimens during the SEM preparation might also have caused a release of residual stress around the voids and subsequently a change of the geometry of the voids.

A relatively low accelerating voltage of 5 keV was used in the SEM to limit the penetration depth of the electron beam. Still, some penetration could not be avoided. This may lead to overestimation of the particle content. The quality of the SEM micrographs is another source of error. With a poor focus, fewer particles are visible in the micrograph. If too much time was used to focus at one point, the material was heated and cracked. Therefore, the SEM process had to be performed rather quickly. The applied zooming level might cause the smallest particles not to appear in the micrographs. Moreover, the considered micrographs had to be sufficiently large in order to depict a representative area fraction of particles and voids. Two micrographs were considered for each specimen during the counting process. These might have been recorded at an area that was not perfectly representative, or they might not have been located exactly at the region of highest deformation. However, the initial particle volume fraction was determined from one SEM micrograph only. It was estimated to be $\omega_0 = 0.24$. This might be a too high figure since it is larger than the particle and void volume fractions estimated for the slightly deformed specimens in Test 1 to Test 3. An initial volume fraction of particles of $\omega_0 \approx 0.2$ is assumed to be more realistic. This is therefore the volume fraction employed in the unit cell model.

It was challenging to determine from the micrographs whether the observed objects were particles, voids or just material irregularities. Different automatic techniques to trace the outlines of the particles and the voids were evaluated (Malvik, 2011). Comparison of the outlines found by the various techniques demonstrated that manual identification was the most accurate one. An alternative method for determination of the void volume fraction is to use X-ray tomography (Cayzac et al., 2013; Laiarinandrasana et al., 2010).

The volume strains plotted in Fig. 4(a) and the retraction ratios plotted in Fig. 4(b) show that the dilation changes during the deformation. Initially, when the particles are well attached to the matrix, the retraction ratio of the composite is determined by the Poisson's ratio of each of the components. When debonding sets in, growth of voids causes dilation at the macroscale, observed as a reduction in the retraction ratio. The retraction ratio has the lowest value at longitudinal strain in the range 0.07–0.10.

Fig. 7(b) shows that the volume strain estimated from SEM micrographs is smaller than those found by DIC. The difference may be related to creep during the time elapsed between the measurements, limited quality of SEM micrographs or by inaccurate estimation of particle and void area fractions from the micrographs. Moreover, there may be a contribution from very small particles that were not traceable at the micrographs.

Particle debonding and void growth can be regarded as damage mechanisms. When a particle debonds from the matrix, the load bearing cross section of the specimen is reduced. Simple expressions for particle debonding and void growth were used to estimate an effective stress in the damaged material. Fig. 8(b) shows that the macroscopic softening disappears in the effective stress–strain curve taking void nucleation and growth into account. Moreover, similar to the findings of Mohanraj et al. (2006), it is seen that the effective stress–strain curve exhibits a more pronounced hardening than the stress–strain curve for the voided material.

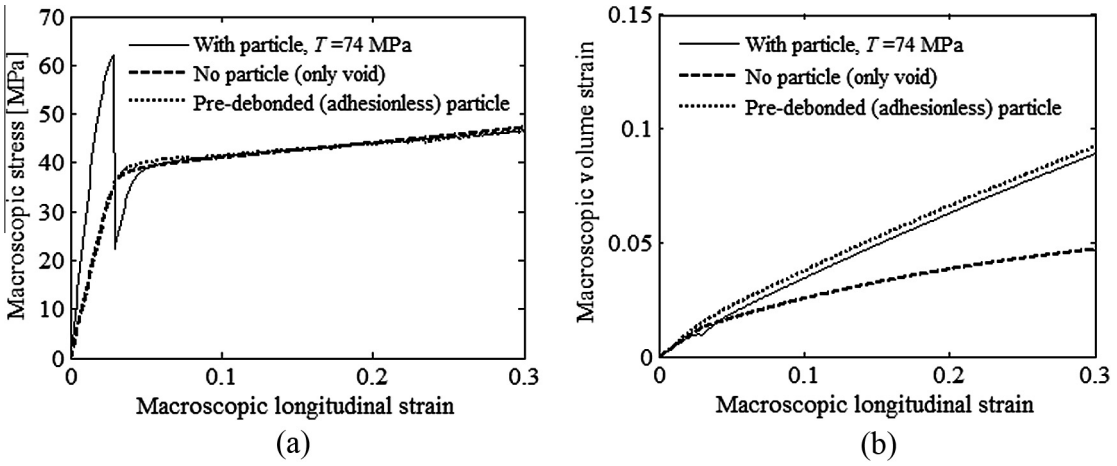

Fig. 16. Results from simulations employing unit cells without cohesive elements and without particle: (a) macroscopic stress–strain curves, and (b) volume strains.

5.2. Numerical study

Crude simplifications in the numerical unit cell model have been done with respect to geometric representation as well as constitutive modelling. Therefore, the behaviour observed in the laboratory tests could not be accurately reproduced. Indeed Williams et al. (2012) demonstrate that modelling with the actual microstructure has a significant influence on debonding of particles and localization of strains in numerical simulations.

The unit cell models were subjected to a macroscopic uniaxial stress state. However, considering that slight necking occurred in the most deformed samples, see Fig. 2, this is not an exact reproduction of the stress state in the laboratory tests. It is well-known that the volume change due to void growth in polymers is highly influenced by the hydrostatic stress state (Cayzac et al., 2013; Laiarinandrasana et al., 2012). Moreover, high stress triaxialities may accelerate particle debonding, void growth and onset of coalescence as found by Yerra et al. (2013) for metallic systems. Subjecting the unit cell models to a stress state with gradually increasing triaxiality throughout the test might give a more realistic response as compared with the laboratory tests. This may serve as an explanation of the underestimation of the volume strains in Fig. 15.

Turning the attention to constitutive modelling of the matrix material, it should be emphasized that the applied material model for the PVC matrix does not incorporate intrinsic softening, pressure dependent flow, intrinsic dilation, strain rate effects or temperature effects. Studies employing more advanced, and more realistic, matrix material models certainly exist in the literature. As an example, the material model originally derived by Boyce et al. (1988) and later modified by Wu and van der Giessen (1996) seems to be commonly used (Pijnenburg and van der Giessen, 2001; Seelig and van der Giessen, 2002, 2009). It is a visco-plastic material model for large strains where the intrinsic softening of the material is taken into account. Including intrinsic softening in the model of the PVC matrix is likely to give even stronger stress-softening on the macro-scale than what is seen in Fig. 12(a). Another consequence of including intrinsic softening is localization of the deformation in the ligaments between the voids. Amongst others, this has been studied by Steenbrink et al. (1997) and Pijnenburg and van der Giessen (2001).

The model employed by Wu and van der Giessen (1996) and others also incorporates pressure dependent yielding of the matrix but assumes isochoric flow. If the matrix material had been modelled as a dilatant material (Guo et al., 2008), the weighted average volume strain from the unit cell simulations, see Fig. 15, might have been closer to the volume strain from the laboratory test.

The maximum local stress occurring in the PVC matrix in the unit cell model is approximately 120 MPa. This level is governed by the strain hardening response of the matrix material as as displayed in Fig. 8(b). It is somewhat higher than the effective stress σ_{eff} estimated by employing Eq. (9), which is plotted by a solid line in the same figure. The stress σ_{eff}, however, is averaged over the ligament, and it is possible that higher stresses occur locally in the PVC matrix of the real composite.

The current study focuses on the damage evolution before final failure, not the final failure itself. Based on the observed mechanisms, it is however natural to suggest two different possibilities. Necking of the ligaments may take place and lead to final failure by void coalescence and collapse of ligaments between the voids, as discussed by, e.g., Steenbrink et al. (1997). In other cases where the strain hardening from orientation and stretching of the polymer network is strong, brittle failure of the ligaments may be the result (Landis et al., 2000).

It should be emphasized that the unit cell model in this study is not intended to replicate the exact behaviour observed in the laboratory tests. The purpose of the unit cell study was rather to investigate the mechanisms behind the deformation. Therefore, the numerical study was intentionally designed in a simple manner so that the key macroscopic features, namely the volume change and the stress softening, easily could be identified and linked to the key microscopic mechanisms, namely particle debonding and void growth. As a result, we clearly see plastic dilation due to void growth. Moreover, it is evident that debonding of particles and void growth induce stress-softening in the unit cell models. These results may be transferred to the interpretation of the laboratory tests. When a statistical distribution of the cohesive strength is taken into account, the shape of the macroscopic stress–strain curve of the unit cell model approaches that from the experimental tests. This means that the peak stress observed in the experiments may be considered as a macroscopic debonding stress rather than a conventional yield stress.

6. Conclusions

The investigated material is a composite of a PVC matrix containing comparatively stiff mineral particles, mainly $CaCO_3$. Debonding of the mineral particles seems to initiate when a certain stress is reached. Thereafter, void growth is a dominating mechanism at the microscale. The observed plastic dilation measured by DIC on the macroscopic scale is in good agreement with the estimated void growth on the microscale. Void growth is therefore concluded to be the main source of the plastic dilation. Both particle debonding and void growth are identified as damage mechanisms in this composite material. Thus, the amount of damage cannot be estimated from the volume change alone; the volume occupied by debonded particles also has to be taken into account.

Despite crude idealizations, some of the mechanical characteristics found in experimental tests are observed in the results from the numerical study; these include the shape of the stress–strain curve and the plastic dilation caused by void growth. The matrix-particle debonding in the numerical model leads to stress-softening of the macroscopic stress–strain curve. The peak stress of the stress–strain curve observed in laboratory tests may also be induced by stress-softening as a result of debonding of particles.

Acknowledgements

The authors want to thank Professor Leon Govaert at Eindhoven University of Technology for providing results from thermogravimetric analyses. Gratitude also goes to Alexander Haugvik Malvik for contribution to this work through his master thesis. The work presented in this paper is a result of cooperation between Karlsruhe Institute of Technology and Norwegian University of Science and Technology that has been possible due to a travel grant through the DAADppp programme from The Research Council of Norway. This research was supported in part with computational resources at NTNU provided by NOTUR, http://www.notur.no.

References

Addiego, F., Martino, J.D., Ruch, D., Dahoun, A., Godard, O., Patlazhan, S., 2011. Quantification of cavitation in neat and calcium carbonate-filled high-density polyethylene subjected to tension. J. Eng. Mater. Technol. 133, 030904.
Argon, A.S., Cohen, R.E., 2003. Toughenability of polymers. Polymer 44, 6013–6032.
Bartczak, Z., Argon, A.S., Cohen, R.E., Weinberg, M., 1999. Toughness mechanism in semi-crystalline polymer blends: II. High-density polyethylene toughened with calcium carbonate filler particles. Polymer 40, 2347–2365.
Boyce, M.C., Parks, D.M., Argon, A.S., 1988. Large inelastic deformation of glassy polymers. Part I: rate dependent constitutive model. Mech. Mater. 7, 15–33.
Cangemi, L., Elkoun, S., G'Sell, C., Meimon, Y., 2004. Volume strain changes of plasticized poly(vinylidene fluoride) during tensile and creep tests. J. Appl. Polym. Sci. 91, 1784–1791.
Cayzac, H.-A., Saï, K., Laiarinandrasana, L., 2013. Damage based constitutive relationships in semi-crystalline polymer by using multi-mechanisms model. Int. J. Plast. 51, 47–64.

Chen, J.K., Huang, Z.P., Zhu, J., 2007. Size effect of particles on the damage dissipation in nanocomposites. Compos. Sci. Technol. 67, 2990–2996.
Chu, C.C., Needleman, A., 1980. Void Nucleation effects in Biaxially Stretched Sheets. J. Eng. Mater. Technol. 102, 249–256.
Delhaye, V., 2010. Behaviour and Modelling of Polymers for Crash Applications. NTNU, Trondheim, Department of Structural Engineering, p. 211.
Delhaye, V., Clausen, A.H., Moussy, F., Hopperstad, O.S., Othman, R., 2010. Mechanical response and microstructure investigation of a mineral and rubber modified polypropylene. Polym. Testing 29, 793–802.
Delhaye, V., Clausen, A.H., Moussy, F., Othman, R., Hopperstad, O.S., 2011. Influence of stress state and strain rate on the behaviour of a rubber-particle reinforced polypropylene. Int. J. Impact Eng. 38, 208–218.
Fu, S.-Y., Feng, X.-Q., Lauke, B., Mai, Y.-W., 2008. Effects of particle size, particle/matrix interface adhesion and particle loading on mechanical properties of particulate–polymer composites. Compos. B: Eng. 39, 933–961.
Galeski, A.A., 2003. Strength and toughness of crystalline polymer systems. Prog. Polym. Sci. 28, 1643–1699.
G'Sell, C., Hiver, J.M., Dahoun, A., Souahi, A., 1992. Video-controlled tensile testing of polymers and metals beyond the necking point. J. Mater. Sci. 27, 5031–5039.
Guo, T.F., Faleskog, J., Shih, C.F., 2008. Continuum modeling of a porous solid with pressure-sensitive dilatant matrix. J. Mech. Phys. Solids 56, 2188–2212.
Hempel, P., Hillenberg, A., Seelig, T., 2010. Micromechanical modeling of talc particle reinforced thermoplastic polymers. Proceedings in Applied Mathematics and Mechanics (PAMM) 10, 293–294.
Kachanov, L.M., 1986. Introduction to Continuum Damage Mechanics. Nijhoff, Dordrecht.
Katz, H.S., Milewski, J.V., 1987. Handbook of Fillers for Plastics. Van Nostrand Reinhold Co., New York.
Kemal, I., Whittle, A., Burford, R., Vodenitcharova, T., Hoffman, M., 2009. Toughening of unmodified polyvinylchloride through the addition of nanoparticulate calcium carbonate. Polymer 50, 4066–4079.
Laiarinandrasana, L., Morgeneyer, T.F., Proudhon, H., Regrain, C., 2010. Damage of semicrystalline polyamide 6 assessed by 3D X-ray tomography: From microstructural evolution to constitutive modeling. J. Polym. Sci., Part B: Polym. Phys. 48, 1516–1525.
Laiarinandrasana, L., Morgeneyer, T.F., Proudhon, H., N'guyen, F., Maire, E., 2012. Effect of multiaxial stress state on morphology and spatial distribution of voids in deformed semicrystalline polymer assessed by X-ray tomography. Macromolecules 45, 4658–4668.
Landis, C.M., Pardoen, T., Hutchinson, J.W., 2000. Crack velocity dependent toughness in rate dependent materials. Mech. Mater. 32, 663–678.
Lay, B., Brunet, M., Boivin, M., 1998. Modelling of void nucleation and fiber debonding in a composite material. J. Mater. Process. Technol. 77, 254–259.
LS-DYNA, 2007. LS-DYNA Keyword User's Manual. Version 971. Livermore Software Technology Corporation (LSTC).
Malvik, A.H., 2011. Void Growth in Calciumcarbonate Filled PVC. NTNU, Trondheim, Department of Structural Engineering, p. 56.
Mishra, S., Perumal, G.B., Naik, J.B., 1997. Studies on mechanical properties of polyvinyl chloride composites. Polymer-Plastics Technology and Engineering 36, 489–500.
Mohanraj, J., Barton, D.C., Ward, I.M., Dahoun, A., Hiver, J.M., G'Sell, C., 2006. Plastic deformation and damage of polyoxymethylene in the large strain range at elevated temperatures. Polymer 47, 5852–5861.
Moura, R.T., Clausen, A.H., Fagerholt, E., Alves, M., Langseth, M., 2010. Impact on HDPE and PVC plates – experimental tests and numerical simulations. Int. J. Impact Eng. 37, 580–598.
Needleman, A., 1987. A continuum model for void nucleation by inclusion debonding. Trans. ASME, J. Appl. Mech. 54, 525–531.
Ognedal, A.S., 2012. Large-deformation behaviour of thermoplastics at various stress states. An experimental and numerical study, Ph.D. thesis. Department of Structural Engineering, NTNU, Trondheim, p. 300.
Ognedal, A.S., Clausen, A.H., Polanco-Loria, M., Benallal, A., Raka, B., Hopperstad, O.S., 2012. Experimental and numerical study on the behaviour of PVC and HDPE in biaxial tension. Mech. Mater. 54, 18–31.
Pijnenburg, K.G.W., van der Giessen, E., 2001. Macroscopic yield in cavitated polymer blends. Int. J. Solids Struct. 38, 3575–3598.
Pinho, S.T., Iannucci, L., Robinson, P., 2006. Formulation and implementation of decohesion elements in an explicit finite element code. Compos. A: Appl. Sci. Manuf. 37, 778–789.
Product Information PVC-TF, in: SIMONA (Ed.), www.SIMONA.com.
Schneider, C.A., Rasband, W.S., Eliceiri, K.W., 2012. NIH Image to ImageJ: 25 years of image analysis. Nat. Methods 9, 671–675.
Seelig, T., van der Giessen, E., 2002. Localized plastic deformation in ternary polymer blends. Int. J. Solids Struct. 39, 3505–3522.
Seelig, T., van der Giessen, E., 2009. A cell model study of crazing and matrix plasticity in rubber-toughened glassy polymers. Comput. Mater. Sci. 45, 725–728.
Socrate, S., Boyce, M.C., 2000. Micromechanics of toughened polycarbonate. J. Mech. Phys. Solids 48, 233–273.
Steenbrink, A.C., van der Giessen, E., 1999. On cavitation, post-cavitation and yield in amorphous polymer–rubber blends. J. Mech. Phys. Solids 47, 843–876.
Steenbrink, A.C., van der Giessen, E., Wu, P.D., 1997. Void growth in glassy polymers. J. Mech. Phys. Solids 45, 405–437.
van Dommelen, J.A.W., Brekelmans, W.A.M., Baaijens, F.P.T., 2003. A numerical investigation of the potential of rubber and mineral particles for toughening of semicrystalline polymers. Comput. Mater. Sci. 27, 480–492.
Vollenberg, P.H.T., Heikens, D., 1990. The mechanical properties of chalk-filled polypropylene: a preliminary investigation. J. Mater. Sci. 25, 3089–3095.
Weibel, E.R., 1979. Stereological Methods – Practical Methods for Biological Morphometry. Academic Press, London.
Williams, J.J., Segurado, J., Llorca, J., Chawla, N., 2012. Three dimensional (3D) microstructure-based modeling of interfacial decohesion in particle reinforced metal matrix composites. Mater. Sci. Eng. A 557, 113–118.
Wu, P.D., van der Giessen, E., 1996. Computational aspects of localized deformations in amorphous glassy polymers. Eur. J. Mech. A/Solids 15, 799–823.
Yerra, S.K., Martin, G., Véron, M., Bréchet, Y., Mithieux, J.D., Delannay, L., Pardoen, T., 2013. Ductile fracture initiated by interface nucleation in two-phase elastoplastic systems. Eng. Fract. Mech. 102, 77–100.